Check for updates

Machine learning of the architecture–property relationship in graft polymers†

Kevin V. Bigting,[a] Jordan J. Carden,[a] Shubhadeep Nag, [b] Jimmy Lawrence, [b] Yen-Fang Su[c] and Yaxin An [*b]

Graft polymers are promising in energy and biomedical applications. However, the diverse architectures make it challenging to establish their structure–property relationships. We systematically investigate how backbone and side-chain architectures influence four key properties: glass transition temperature (T_g), self-diffusion coefficient (D), radius of gyration (R_g), and packing density (ρ). Using molecular dynamics simulations, we analyze a dataset of 500 graft polymers with randomly positioned side chains. T_g and D exhibit decoupled relationships due to the distinct topological effects. Furthermore, we develop dense neural networks (DNNs) and convolutional neural networks (CNNs) to pave the way to polymer design with desired properties.

Graft polymers consist of a main backbone with one or more side chains, giving them combined or novel properties not found in linear or block copolymers.[1–3] Their architecture enables enhanced or unique material functionalities. Bottlebrush architectures, a special class of graft polymers, feature highly grafted side chains that suppress molecular entanglements, yielding materials softer than conventional elastomers. These polymers have emerged as pivotal materials in advanced 3D printing, enabling solvent-free fabrication of ultra-soft elastomers with biomimetic mechanical properties that mimic biological tissues.[4] To optimize printability, shape retention, and post-print functionality, precise engineering of their thermal properties and dynamics is essential.

The glass transition temperature (T_g) is a fundamental thermal property of graft polymers that governs their printability.[5] It defines the temperature at which a polymer transitions from a rigid to a rubbery state, influencing the flow behavior, shape retention, and post-print structural integrity in 3D printing.[6] Previous experimental studies have shown that T_g depends on both the chemical composition and the architectural arrangement of the backbone (N_{bb}) and side chain (N_{sc}) lengths.[7,8] Additionally, recent advances based on the generalized entropy theory (GET)[9] have demonstrated that the relative rigidities of the backbone and side chains critically influence the glass formation behavior in graft polymers.[10] These theoretical predictions, supported by molecular dynamics (MD) simulations[11] and experimental studies,[12] reveal the nontrivial trends in T_g.

Besides the thermodynamic property T_g, the dynamical property, such as polymer diffusion in the melt state, is crucial to their processing, *e.g.* governing interlayer bonding in 3D printing, material homogeneity, and mechanical performance.[13,14] During extrusion-based 3D printing, molten polymer layers must interdiffuse to form entangled molecular networks and strong interlayer bonds.[5] The self-diffusion coefficient (D) of a polymer is influenced by molecular weight, backbone rigidity, and side-chain length.[15,16] Shorter, flexible side chains generally promote faster diffusion by reducing entanglements, while longer, rigid side chains hinder diffusivity, increasing viscosity and reducing chain relaxation dynamics.[15]

However, a comprehensive understanding of T_g and the diffusion of graft polymers is still lacking due to their diverse structures.[7,17] In this study, we address the long-standing challenge of predicting polymer thermal and dynamical properties based on their molecular architectures, driven by the highly nonlinear and complex structure–property relationships in polymers.[18] Despite extensive experimental and computational efforts,[19–21] the vast combinatorial space of backbone and side-chain configurations makes it difficult to establish generalizable design principles. The design parameters such as N_{bb}, N_{sc}, grafting density (f), and spatial positioning of side chains play a crucial role in shaping polymer behavior. A thorough investigation is carried out here by investigating 500 graft polymers with randomly placed side chains to understand how graft polymer architectures impact thermal and dynamic properties. By identifying key trends, we aim to establish a

a Department of Computer Science and Engineering, Louisiana State University, Baton Rouge, LA 70803, USA

b Department of Chemical Engineering, Louisiana State University, Baton Rouge, LA 70803, USA

c Department of Civil and Environmental Engineering, Louisiana State University, Baton Rouge, LA 70803, USA

This journal is © the Owner Societies 2025

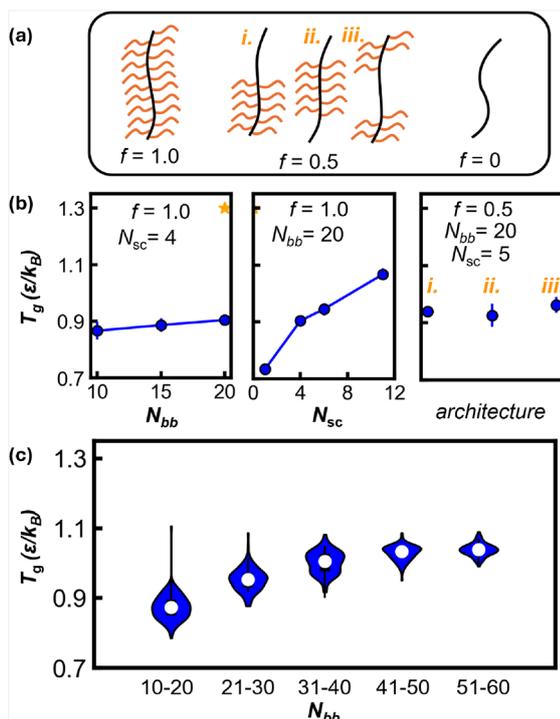*Phys. Chem. Chem. Phys.*, 2025, **27**, 13243–13247 | **13243**

Fig. 1 (a) Schematic representation of graft polymers is shown here for fully grafted ($f = 1.0$) and partially grafted polymers ($f = 0.5$) along with a linear polymer ($f = 0$). For $f = 0.5$, three distinct side-chain architectures (*i.*, *ii.*, and *iii.*) are illustrated. (b) The variation of T_g is shown for $f = 1.0$ and 0.5 with respect to backbone length (N_{bb}), side-chain length (N_{sc}), and side-chain architecture. The T_g of a classical linear polymer ($f = 0$) is included as a reference (orange star). (c) The glass transition temperatures of 500 randomly generated graft polymers are plotted as a function of N_{bb}, capturing the broader distribution of T_g values across various molecular architectures.

framework for designing graft polymers with optimal thermal and dynamic performance.

We began by examining polymers with different grafting densities, including fully grafted bottlebrush polymers ($f = 1.0$), partially grafted polymers ($f = 0.5$), and classical linear polymers ($f = 0$), as illustrated in Fig. 1(a). To investigate the influence of N_{bb} and N_{sc} on T_g, we simulated a total of 500 graft polymers, with 10 polymers at each value of f from 0.1 to 1.0 across five backbone-length blocks (10–20, 21–30, 31–40, 41–50, 51–60). The side-chain length is randomly generated. The value of T_g is obtained from density analysis as a function of temperature. More computational details are provided in Section S1 of the ESI.†

As shown in Fig. 1(b), left panel, the variation of T_g with backbone length is minimal for bottlebrush polymers with $N_{sc} = 4$, increasing only slightly from 0.87 to 0.9 ε/k_B as N_{bb} increases from 10 to 20. The slight impact of N_{bb} on T_g may be attributed to the narrow range of N_{bb} from 10 to 20. Besides, N_{sc} has a pronounced effect, as seen in Fig. 1(b), middle panel, where T_g increases from 0.73 to 1.07 ε/k_B as N_{sc} increases from 1 to 11 for a bottlebrush polymer with $N_{bb} = 20$. To establish a baseline comparison, we also computed T_g for a linear polymer, which is significantly higher ($T_g = 1.3$ ε/k_B) than that of

bottlebrush ones. This is consistent with the trend observed in experimentally synthesized bottlebrush polystyrene,[7] where, the T_g of bottlebrush polystyrene increases from 37 °C to 87 °C as N_{sc} increases from 2 to 8. The T_g values are found to be much smaller than those of linear polystyrene (90–110 °C).[22]

Beyond N_{bb} and N_{sc}, we analyzed the effects of another key design parameter, the side-chain positioning, as illustrated in Fig. 1(b), right panel. The side chains are positioned at one end (*i.*), the center (*ii.*), and both ends (*iii.*), while keeping $N_{bb} = 20$ and $N_{sc} = 5$ constant. Differences in T_g among these architectures are minimal, consistent with experimental findings by Dearman *et al.*[7] Their synthesized bottlebrush polystyrene analogs, including types (*i.*), (*ii.*), and (*iii.*), showed a T_g variation of ≤ 5 K, supporting our results.

To examine the global trend in T_g, we plotted the variation of the average T_g as a function of N_{bb} in Fig. 1(c). The results show that T_g increases progressively as N_{bb} increases from 10 to 40, beyond which it reaches a plateau (from 41 to 60), indicating that further backbone elongation has little impact on T_g. These results demonstrate that the glass transition temperature of graft polymers is strongly influenced by both N_{sc} and N_{bb}, with N_{sc} playing a more dominant role at low N_{bb}. While increasing N_{bb} leads to a moderate rise in T_g, this effect saturates beyond $N_{bb} = 40$. In contrast, longer side chains significantly enhance T_g, suggesting that side-chain flexibility and steric effects play a crucial role in determining the thermal behavior of these polymers, as evident from literature based on the GET framework.[10,11] The influence of chain rigidity on T_g was further investigated by varying the angular force constant k_θ, as detailed in Section S2 of the ESI.† Next, we examine the diffusivity of graft polymers in the melt state.

In classical polymer physics, D is inversely related to the hydrodynamic radius (R_h) through the Stokes–Einstein relation.[15] Since R_h is proportional to the radius of gyration (R_g) in polymeric systems ($R_h/R_g \approx 0.9$–1.0),[16] we focus on the relationship between D and R_g here. These values are obtained from simulations run at $T = 2.0$ ε/k_B specifically at the melt state of polymers.

Fig. 2(a) presents the variation of R_g for graft polymers compared to linear ones, where the backbone length of linear polymers varies from 10 to 90. By plotting the *x*- and *y*-axes of Fig. 2(a) in logarithmic scale, we computed the slope of the variation of R_g of linear polymers with changes in N_{bb}, resulting in a value of 0.66. This observed exponent is larger than that of an ideal random-walk polymer ($R_g \propto N_{bb}^{0.5}$),[15] which can be attributed to the increased rigidity of the bead-spring model used in this work.

For polymers with f values of 0.5 and 1.0, the relationship between R_g and N_{bb} deviates significantly from the power-law trend observed for linear polymers. The dependence of R_g on polymer side-chain architecture is found to be scattered with no definite trend, particularly with respect to N_{sc} and its spatial distribution along the backbone. When N_{sc} is short (1 and 4), the R_g of bottlebrush polymers is smaller than that of a linear polymer with $N_{bb} = 20$, indicating a more collapsed polymer conformation due to attractive interactions between short side chains. As N_{sc} increases to 6, R_g becomes comparable to that of

13244 | *Phys. Chem. Chem. Phys.*, 2025, **27**, 13243–13247

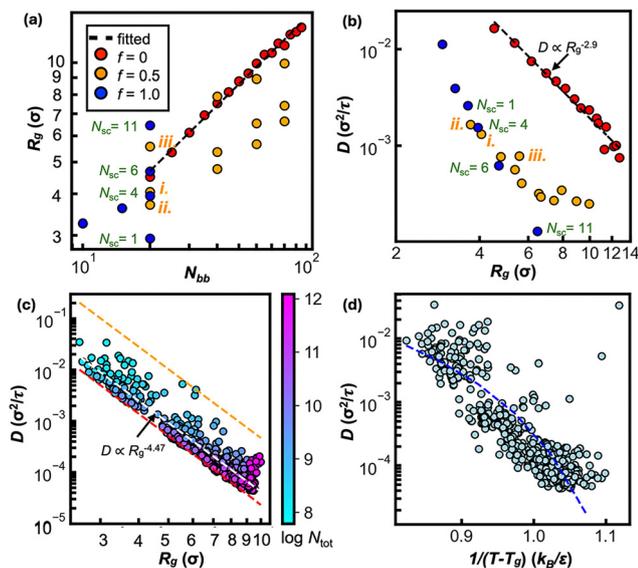This journal is © the Owner Societies 2025

Fig. 2 (a) Radius of gyration (R_g) of linear polymers ($f = 0$) and graft polymers ($f = 0.5, 1.0$). The dashed line represents a power law scaling as $N_{bb}^{0.66}$. (b) Self-diffusion coefficient (D) of linear and graft polymers. The dashed line represents a power law scaling as $R_g^{-2.9}$. (c) The relationship between D and R_g of all the 500 graft polymers. The white dashed line represents the power scaling, $R_g^{-4.47}$. The red and yellow dashed lines are the lower and upper boundaries of the 500 data points. (d) The D vs. $1/(T - T_g)$ relationship deviates far from the WLF equation with $T_1 = 0$ (the blue dashed line).

a linear polymer, suggesting a transition from a collapsed to an expanded state. When N_{sc} further increases to 11, steric hindrance between the long side chains leads to an expanded conformation, where R_g exceeds that of a linear polymer. Apart from N_{sc}, the spatial placement of side chains also affects R_g. Among the three configurations analyzed in Fig. 1(a), graft polymers with configuration (*ii.*) exhibit the most collapsed structure, followed by configuration (*i.*), while configuration (*iii.*), where side chains are positioned at both ends, resulting in the most extended backbone conformation.

Next, we examine the relationship between R_g and D for linear and graft polymers. Note that the diffusion coefficient is computed from the mean-squared displacement of the polymer chain's center of mass, indicating that the diffusion discussed here refers to chain-level motion. We assume the behaviors of polymers in this study are in the unentangled regime because the maximum backbone length ($N_{bb} = 60$) is less than the reported entanglement length N_e of 86.[16,23] As shown in Fig. 2(b), for linear polymers, D follows a power-law scaling as $D \propto R_g^{-2.9}$, which is comparable to $D \propto R_h^{-2.7}$ reported in ref. 16. For graft polymers, D is significantly lower than that of linear polymers at the same R_g. While D decreases with increasing R_g, similar to linear polymers, the data points for graft polymers do not collapse onto a single power-law trend, indicating that a simple scaling relationship does not adequately describe their diffusivity. Fig. 2(c) and (d) reveal key deviations from classical scaling and transport theories in graft polymers. In Fig. 2(c), although an overall trend of $D \propto R_g^{-4.47}$ is

observed, the significant spread in D at fixed R_g demonstrates a breakdown of universal diffusion-size relationships due to topological factors. Fig. 2(d) shows that D does not follow the expected behavior from the Williams–Landel–Ferry (WLF) equation, $\log D = -C_1 \log D(T_1)/(C_2/(T - T_g + T_1) + 1)$ where C_1 and C_2 are constants,[24] as polymers with similar T_g exhibit diffusion rates differing by orders of magnitude, highlighting a decoupling between dynamic and thermodynamic properties enabled by architectural control.

The structural diversity introduced by side chains in our MD simulations leads to substantial variations in chain mobility, highlighting the need for a more comprehensive model to describe the diffusion behavior of graft polymers in the melt state.

Accurately predicting the T_g and D is therefore challenging due to their nonlinear structure–property relationships. To overcome this, we developed machine learning (ML) models trained on simulated polymer datasets. A key aspect here is the featurization strategy, which plays a critical role in model performance. We tested three types of polymer representations: (1) six physical descriptors, (2) eleven graphical descriptors,[25] and (3) two-dimensional grayscale images. Dense neural network (DNN) models were implemented for the first two feature sets, while convolutional neural networks (CNN) were developed for image-based representations (see Section S3 of ESI† for model descriptions).

Before training the ML models, we examined the correlation between physical and graphical descriptors to assess feature relevance. Fig. S3 (ESI†) presents the Spearman's rank correlation coefficients, where most of the physical and graphical descriptors are highly correlated with the four properties.

By utilizing the physical descriptors or the graphical descriptors, we trained DNN models for each of these properties. The hyperparameters of DNN models are optimized, *i.e.* the number of hidden layers, the number of hidden nodes, and the learning rate to improve the accuracy (see Section S3.2 of ESI†). The DNN model consisted of 4 hidden layers and each hidden layer contained 512, 1024, 512, and 32 hidden nodes. The learning rate is 0.001 and the activation function is rectified linear unit. The 10-fold cross-validation is used to get the average values of the R^2 scores on testing datasets. The R^2 scores of the DNN models by using the physical descriptors for predicting T_g, R_g, D, and ρ are shown in Fig. 3. All the R^2 scores are more than 0.9, except for T_g. However, it is noted that though the R^2 score for predicting T_g is 0.85, the root mean square error is found to be 0.025 as obtained from MD simulations. Overall, the DNN models trained on graphical descriptors perform slightly better than those trained on physical descriptors. This is because physical descriptors are limited in differentiating the configurations of graft polymers. For example, the configurations of (*i.*) (*ii.*) and (*iii.*) in Fig. 1(a) are represented by the same six physical descriptors.

Besides the physical and graphical descriptors, we used 26×60 pixels (corresponding to maximum N_{sc} and N_{bb} in the dataset) grayscale images to represent graft polymers. Pixels in the matrix indicated different types of beads: black pixels (grayscale value = 0) denoted backbone beads, gray pixels
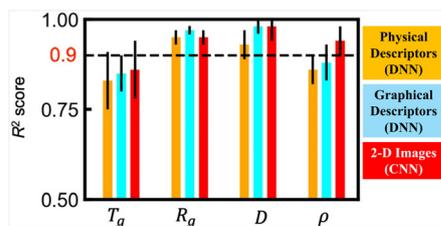
This journal is © the Owner Societies 2025

Phys. Chem. Chem. Phys., 2025, **27**, 13243–13247 | **13245**

Fig. 3 The testing R^2 scores for predicting T_g, R_g, D, and ρ are shown, with a dashed reference (in black) line at 0.9. Orange: DNN models trained on 6 physical descriptors; cyan: DNN models trained on 11 graphical descriptors; red: CNN trained against 26×60 pixels grayscale images. Error bars indicate standard deviations from 10-fold cross-validation.
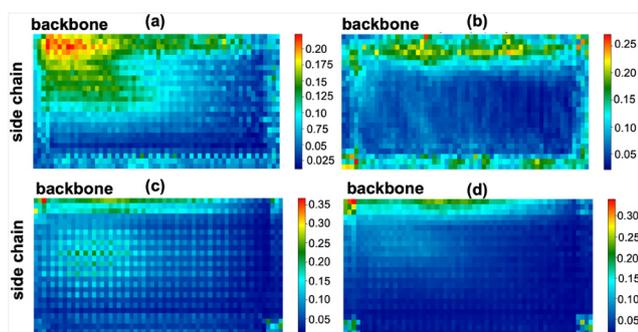

Fig. 4 The average saliency maps across all the 500 samples to show the consistent regions of the graft polymers critical for the four properties: (a) T_g, (b) R_g, (c) D, and (d) ρ. Colors in the colorbar denote the corresponding contribution values of each pixel in the graft polymer images.

(grayscale value = 127) represented side-chain beads, and white pixels (grayscale value = 255) indicated the absence of beads. A representative example of the image for a bottlebrush polymer ($f = 1.0$) with a backbone length of 58 is shown in Fig. S4 of ESI.† The CNN models are trained on these images as the input. The convolutional and pooling layers are optimized (see Section S3.3 of ESI†). The R^2 scores for D, R_g, and T_g are comparable to that of DNN models (Fig. 3). The R^2 score of the CNN model for predicting ρ is 0.94, much higher than that of the DNN model. The R^2 score of our CNN model for predicting R_g is shown comparable to that of GNN models, employed in Jiang et al.[25]

To gain new insights and improve the interpretability of the CNN model, we plotted the saliency map (Fig. 4) highlighting the spatial regions most influential to the CNN model predictions. For T_g, contributions are concentrated at the backbone and nearby side chains, while R_g is driven by both backbone and terminal regions of long side chains. In contrast, D and ρ are primarily influenced by the backbone, reflecting its role in governing steric effects and free volume. A detailed description of the map is given in Section S4 of the ESI.† Further discussion of the general design rules is provided in Section S5 of the ESI.†

In conclusion, our systematic investigation of 500 graft polymers demonstrates that T_g, D, R_g, and ρ are strongly influenced by the nonlinear interplay between backbone and side-chain architectures. These dependencies extend beyond the predictive capabilities of traditional polymer physics models, such as power scaling laws and WLF functions. Notably, T_g and D respond differently to topological variations: D is highly sensitive to the positioning of side chains, whereas T_g is only marginally affected. This differential sensitivity results in a decoupling of T_g and D, thereby overcoming the intrinsic coupling observed in linear polymers that typically constrains the processing of materials with high T_g and low D. The ability to decouple T_g and D enables the rational design of polymers with reduced T_g yet maintained low diffusivity (high viscosity), or vice versa. Additionally, the machine learning models developed in this study accurately and efficiently predict T_g and D, facilitating the topological design of graft polymers to achieve targeted thermodynamic and dynamic properties. In the future, chemically specific models will be developed to guide experimental efforts in validating the ML predictions and synthesizing new graft polymers.

Conflicts of interest

There are no conflicts to declare.

Data availability

The data supporting this article have been included as part of the ESI.†

Notes and references

1 W. F. Daniel, J. Burdyńska, M. Vatankhah-Varnoosfaderani, K. Matyjaszewski, J. Paturej, M. Rubinstein, A. V. Dobrynin and S. S. Sheiko, Nat. Mater., 2016, 15, 183–189.

2 Y. Adeli, T. Raman Venkatesan, R. Mezzenga, F. A. Nüesch and D. M. Opris, ACS Appl. Polym. Mater., 2024, 6, 4999–5010.

3 H. Liang, Z. Wang, S. S. Sheiko and A. V. Dobrynin, Macromolecules, 2019, 52, 3942–3950.

4 P. Xu, S. Wang, A. Lin, H.-K. Min, Z. Zhou, W. Dou, Y. Sun, X. Huang, H. Tran and X. Liu, Nat. Commun., 2023, 14, 623.

5 Z. Jiang, B. Diggle, M. L. Tan, J. Viktorova, C. W. Bennett and L. A. Connal, Adv. Sci., 2020, 7, 2001379.

6 J. Paturej, S. S. Sheiko, S. Panyukov and M. Rubinstein, Sci. Adv., 2016, 2, e1601478.

7 M. Dearman, N. D. Ogbonna, C. A. Amofa, A. J. Peters and J. Lawrence, Polym. Chem., 2022, 13, 4901–4907.

8 K. K. Bejagam, C. N. Iverson, B. L. Marrone and G. Pilania, Phys. Chem. Chem. Phys., 2020, 22, 17880–17889.

9 W.-S. Xu, J. F. Douglas and Z.-Y. Sun, Macromolecules, 2021, 54, 3001–3033.

10 X. Xu, J. F. Douglas and W.-S. Xu, Macromolecules, 2021, 54, 6327–6341.

11 W.-S. Xu, J. F. Douglas and X. Xu, Macromolecules, 2020, 53, 4796–4809.

12 B. Jakobi, K. J. Bichler, F. Juranyi and G. J. Schneider, J. Chem. Phys., 2024, 160, 084901.

13 N. P. Levenhagen and M. D. Dadmun, ACS Appl. Polym. Mater., 2019, 1, 876–884.

13246 | Phys. Chem. Chem. Phys., 2025, 27, 13243–13247

This journal is © the Owner Societies 2025

14 R. Karmakar, N. Venkatareddy, Himanshu, M. Valsecchi, P. K. Maiti, S. Sastry, S. K. Kumar and T. K. Patra, *Soft Matter*, 2025, **21**, 348–355.

15 M. Rubinstein and R. H. Colby, *Polymer physics*, Oxford University Press, 2003.

16 A. Chremos, C. Jeong and J. F. Douglas, *Soft Matter*, 2017, **13**, 5778–5784.

17 J. N. Sevening, N. Nupnar, S. Adhikary, D. Reifsnyder Hickey, M. T. Swulius, H. Koerner, M. J. Hore and R. J. Hickey, *Macromolecules*, 2024, **57**, 9616–9626.

18 J. Shi, Q. Dong, T. Yang and W. Li, *Phys. Chem. Chem. Phys.*, 2025, **27**, 6465–6472.

19 Z. Zhu, J. Hao, Z. Zhang and J. Yang, *Polymer*, 2025, **323**, 128176.

20 G. Chen, L. Tao and Y. Li, *Polymers*, 2021, **13**, 1898.

21 I. V. Mikhailov, E. B. Zhulina and O. V. Borisov, *Phys. Chem. Chem. Phys.*, 2020, **22**, 23385–23398.

22 A. Panwar, V. Choudhary and D. Sharma, *J. Reinf. Plast. Compos.*, 2013, **32**, 740–757.

23 R. S. Hoy, K. Foteinopoulou and M. Kröger, *Phys. Rev. E*, 2009, **80**, 031803.

24 M. E. Yildiz and J. L. Kokini, *J. Rheol.*, 2001, **45**, 903–912.

25 S. Jiang, A. B. Dieng and M. A. Webb, *npj Comput. Mater.*, 2024, **10**, 139.

This journal is © the Owner Societies 2025

Phys. Chem. Chem. Phys., 2025, **27**, 13243–13247 | **13247**